

Microtensile testing and 3D imaging of hydrated Portland cement

P. Trtik & P. Stähli

Institute for Building Materials (IfB), ETH Zurich, 8093 Zurich, Switzerland

E. N. Landis

Department of Civil and Environmental Engineering, University of Maine, Orono, Maine, USA

M. Stampanoni

Swiss Light Source, Paul Scherrer Institute, 5232 Villigen, Switzerland

J. G.M. van Mier

Institute for Building Materials (IfB), ETH Zurich, 8093 Zurich, Switzerland

ABSTRACT: Portland cement has an extremely complex microstructure that defies simple characterizations. While electron microscopy has provided valuable insight on microstructure development, the 2D nature of the data and the required specimen preparation steps continues to provide controversy as to what is real and what is artifact (see for example Diamond (2004a,b) and Scrivener (2004)). Here we present the results of synchrotron-based microtomographic investigations of 130 μm diameter cement specimens subject to uniaxial tension. With the quantitative 3D image analysis of the tomographic data we are able to isolate the different phases, and identify the relationship between the phases and the resulting fracture path. In particular, we see that the crack path shows little if any preference for phase, undermining the notion that at small scales, unhydrated cement grains act as hard aggregates in hydrated cement matrix.

1 INTRODUCTION

At micro-scale cement is composed of various hydrate phases (Calcium Silicate Hydrates (CSH) of various densities, etc.), un-hydrated cement grains (built-up from the different types of clinkers), Calcium Hydroxide (CH), (latently hydraulic) fillers like micro-silica at [nm] and [μm] size, pores of varying size and water. These phases arrange themselves in a random array. In assessing mechanical properties of hydrated cement, the heterogeneity leads us to use test methods that average over representative volumes, or, alternatively, extremely local test methods should be used at scales where the constituting phases can be considered homogenous.

Traditionally, there has always been a trade-off in microstructural measurement techniques. Electron microscopy, in its various forms, has been applied to problems of cement microstructure for more than 25 years (Scrivener (1984)). Especially when combined with energy dispersive X-ray spectroscopy (EDX) (Xu and Sarkar (1991)), insight into the distribution of phases has been invaluable. However, the 2D nature of the data means that important structural information is lost. Recent advances in synchrotron-based X-ray microtomography (SR μ CT), see Stampanoni et al. (2002), have allowed us to produce 3D

images at a spatial resolution beginning to approach that of the electron microscope. In addition, SR μ CT allows the samples to be tested non-invasively in an ambient environment.

Figure 1 illustrates the exploitation of the different techniques. Figure 1a shows a micrograph of cement paste that clearly shows not only distinction between the hydrated (grey) and unhydrated (white) cement phases, and pore space (black), but subtle variations within the unhydrated cement particles are a result of the different compounds that make up the cement clinker. Figure 1b shows a representative slice from a 3D microtomographic image of a similar cement paste. The image also presents the hydrated and unhydrated cement phases, as well as pore space at spatial resolution of 0.7 μm . However, through simple threshold-based image segmentation, we are able to quantify and visualize the distributions of phases in three dimensions. Voids (Figure 1c), unhydrated cement grains (Figure 1d), and the relationship between the two (Figure 1e) are all visible in the volume.

In the work presented here, microtomographic imaging was exploited to examine fracture characteristics of cement pastes at the micron scale. The important issue to be addressed is tensile fracture under a properly defined state of stress. This approach is counter to the current popularity of indentation testing (Shuh et al. (2005), Velez et al. (2001) and Constantinides and Ulm (2004)), which while suitable for homogeneous materials or homogeneous phases,

Pavel Trtik moved in 2006 to the Institute of Mechanical Systems at ETH-Zurich; Eric N. Landis was on sabbatical leave from the University of Maine, and collaborated in the experiments presented in this paper during his stay at IfB.

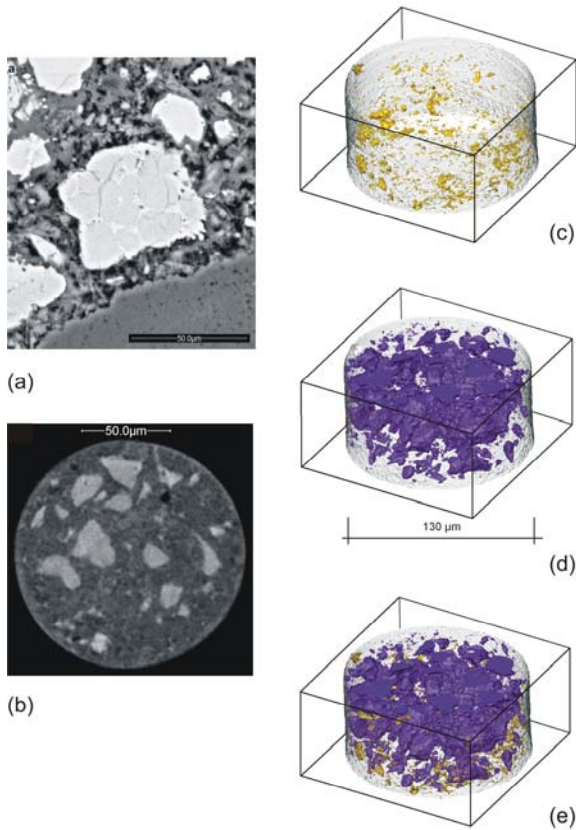


Figure 1. Comparison of ESEM and SR μ CT: (a) Micrograph of the polished surface of hydrated Portland cement. (b) Axial slice from 3D SR μ CT reconstruction of a cylindrical specimen of hydrated Portland cement. 3D-reconstruction of voids (c), unhydrated cement grains (d), and the relationship between the two (e) in part of the volume of 130 μ m-diameter specimen.

appears to be ill-suited for materials like cement and concrete, where the size of indents may be at the scale of material disorder. The high stress concentration of the indenter can lead to compaction of pore space, pop-out of material at indentation edges, and a continuously changing state of stress due to local material changes. Tensile testing results tend to be easier to interpret. Following extensive past experience in the field of tensile testing of concrete and rock at the macro-scale (van Vliet and van Mier (2000), using sample sizes in the range of 50-1600 mm), additional insight was sought at a scale 1000 times smaller. At this scale cement is highly heterogeneous, with “aggregates” consisting of approximately 5-30 μ m unhydrated cement grains. This can be contrasted with the concrete samples tested at the macro-scale where aggregates are in the range of 4-32 mm. Of interest here is the preference of the crack growth towards different phases, and whether there are weak interfaces to direct the crack growth.

2 TEST PROCEDURE

In order to test tensile specimens at a scale approaching 100 μ m, a small loading device was built based on piezoelectric actuation. As illustrated in

Figure 2a, a 15 mm tubular piezoelectric element was mounted to a base fixture. Above this element was a 1.2 mm diameter glass capillary. Tungsten needles are glued to the top and bottom of the 130 μ m diameter cylindrical specimen. This ‘tungsten-cement’ assembly is inserted through the capillary and piezo stack, and glued to the base of the device. As a final step, the top of the top tungsten needle is glued to the top of the capillary. When voltage is applied to the piezoelectric element its expansion results in a tensile loading of the ‘tungsten-cement’ assembly. Prior to assembly, the cement specimen was circumferentially notched at its centre to ensure that cracks would propagate through the material and not at the glue line where stress concentrations occur. The notch was made using femtosecond laser pulses while the specimen was rotating about its principal axis. Figure 2b shows a photograph of the entire tensile device mounted in front of the X-ray detector.

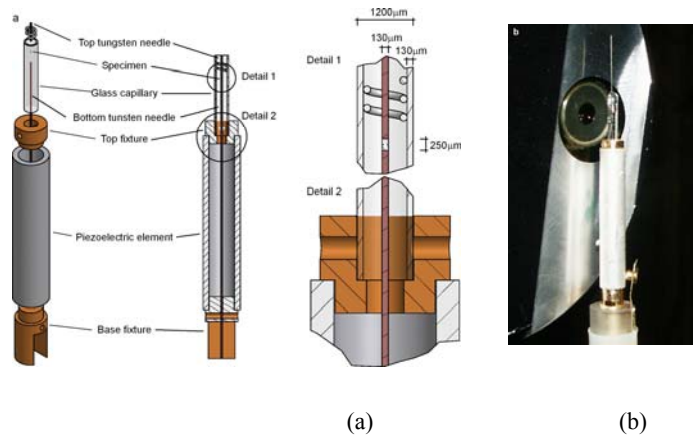


Figure 2. In-situ SR μ CT microtensile testing device: (a) Schematic view of the microtensile device based on piezoelectric actuation, and (b) Photograph of the device in front of the SR μ CT detector

Details of the specimen preparation, the synchrotron X-ray computed microtomography and the applied image analysis techniques are given in the appendix at the end of the paper.

3 FRACTURE PROCESS

Figures 3a to 3c provide visual comparison of tomographic data by showing the equivalent 2D cross-sections of one of the tested specimen at different stages of loading. The corresponding binary images are fitted with the results of the displacement vector field analyses. These fields provide information about the internal displacement fields between the respective loading stage and the specimen in an unloaded state. In stage ‘A’ the specimen is still in the elastic regime showing fairly uniform displacement vector field indicating in particular the occurrence of rigid body motion of the entire specimen

between the unloaded stage and stage 'A' (see Figure 3d). The further stages ('B' and 'C') show cross-section of the crack exhibiting bridging and branching phenomena. The corresponding displacement vector fields for the loading stages 'B' and 'C' show a distinct difference in the direction of the displacement vectors in the regions above and below the crack due to the crack opening (see Figures 3e-3f).

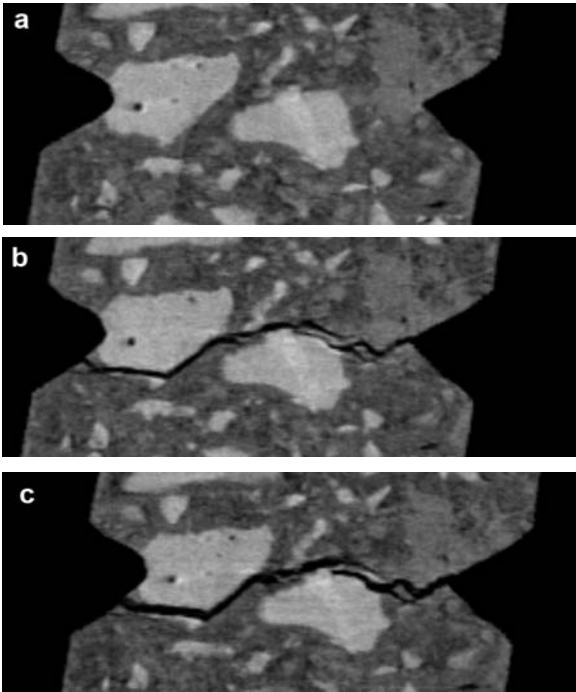


Figure 3a-c. 2D crack reconstructions, displacement vector fields and crack bridging: (a-c) 2D vertical slices from 3D SR μ CT reconstruction of the notched area of the same specimen for three subsequent loading stages ('A', 'B' and 'C').

Also, clear non-uniformity of the displacement vector fields in the vicinity of the crack is observed that can be possibly explained by the existence of strains in the vicinity of crack bridges. The thickness of some of the bridges and the widths of some crack branches is apparently below 1 micrometer (see Figure 3g). Also, the size and shape of the crack bridges can be assessed and visualized in 3D (see Figures 3h-3k). As similar bridging mechanisms were observed in concrete on the macroscale (van Mier (1991)), we suggest that hydrated Portland cement exhibits - when tested on this scale - quasi-brittle post-peak behaviour in the load versus displacement diagram.

4 CRACK SURFACE AREA

As crack surface area is fundamental in fracture, we focus our attention on its measurement (see Table 1). In our binary images (Figures 3d-3f), the largest zero (black) object is the specimen exterior. When the specimen becomes cracked, and the crack connects with the exterior, they combine into a single object.

Thus we can follow changes in cracking by tracking the size of the largest object. Two independent measurements of the crack surface area were carried

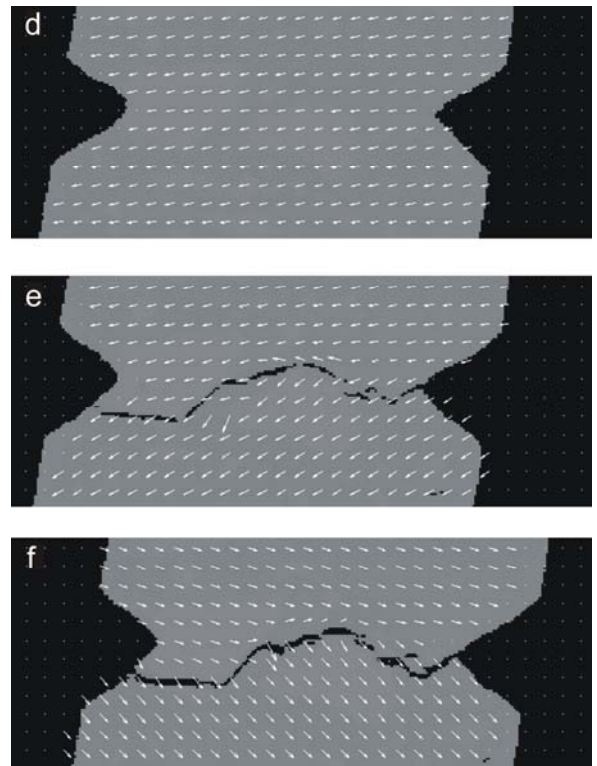


Figure 3d-f. Vector fields showing the displacement between the respective loading stage ('A', 'B' or 'C') and the unloaded state of the specimen.

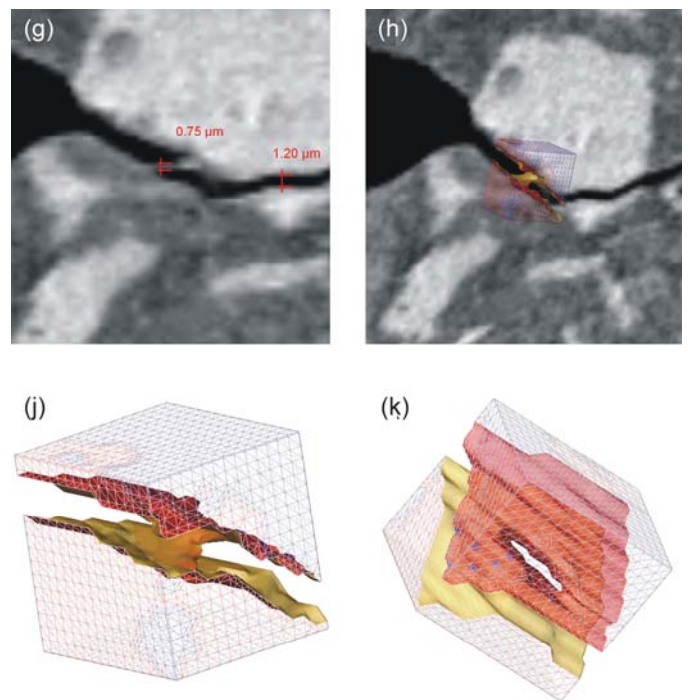


Figure 3g-k. Detail of one of the vertical slices showing one of the bridging events with the sizes of the bridge and crack in micrometers; (h-k) 3D reconstruction of the bridge shown in Figure 3g

out (for identical threshold values between exterior and sample interior). While the larger value of the surface area measurement is determined by adding up the number of boundary free voxel faces (i.e. the voxel faces dividing the exterior and material), the smaller value is the area of the respective 3D surface model of the specimen. As triangular elements are basic building blocks of such 3D surface models, the ratio between the two presented values for the surface area has to remain below $\sqrt{3}$. At the same time we suggest that these values represent the upper and the lower bounds for assessment of the crack surface area. As a point of reference, the nominal specimen cross section at its narrowest point is $7700 \mu\text{m}^2$.

Table 1. Crack volumes and crack surface areas for the stages shown in Figures 3a-3c.

Loading stage	Voltage [V]	Calculation based on count of voxel faces		Calculation based on 3D triangular model	
		ΔV [μm^3]	ΔA [μm^3]	ΔV [μm^3]	ΔA [μm^3]
O	0.0	77	178	101	157
'A'	71.0	29798	23673	29805	18727
'B'	138.0	17182	2425	17161	394
'C'	290.0				

5 THREE-DIMENSIONAL RECONSTRUCTION

Figure 4a shows the total volume of void in the specimen. The 3D reconstructions confirmed that no detectable fracture occurred outside the notch area. Even though it may appear that the majority of crack path shown in two dimensional cross-sections in Figures 3b and 3c followed the interfaces between the unhydrated cement particles and the hydration products, the full reconstruction of the crack surface (Figures 4c-4d) clearly proves that this is not the case in 3D. At the same time, the results suggest that the positions of the crack bridges seem to have no apparent preferential occurrence with regard to the cement microstructure.

It was recently shown that the fracture process in disordered quasi-brittle materials can be simulated by simple models (Herrmann et al. (1989)), in which the fracturing occurs at those locations where stress over strength is most critical in the structure of the material. Such models effectively describe the behaviour of concrete and sandstone (Lilliu and van Mier (2003)) provided that a realistic material structure is indicated instead of a statistical distribution of element properties. Based on the presented results, it

seems to be likely that should the same modelling methodology be extended to smaller scales, i.e. fracture in hydrated Portland cement, the internal microstructural characteristics of unhydrated cement grains will have to be taken into account since they are in the same size range as other elements in the microstructure.

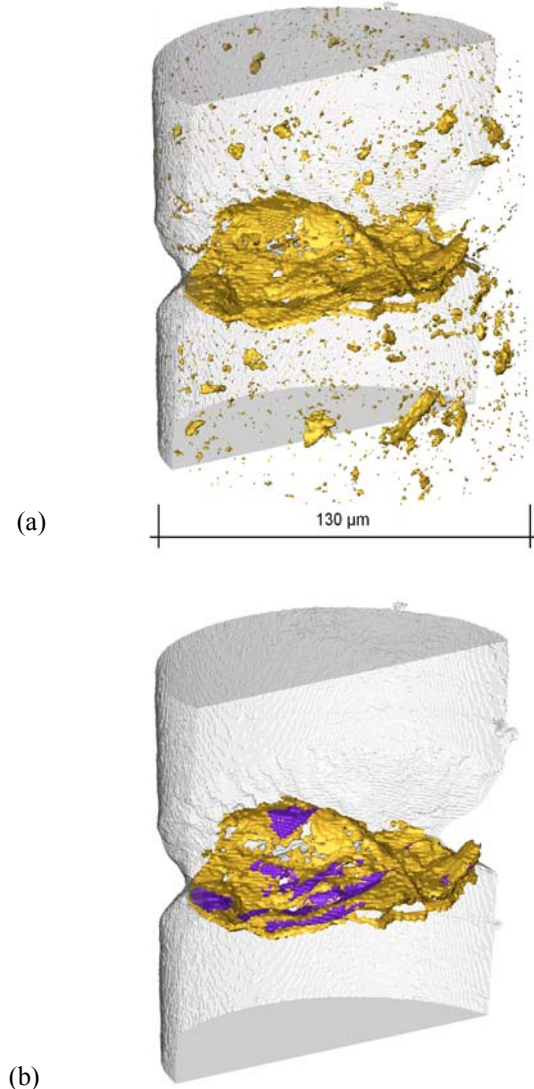


Figure 4. 3D reconstruction of crack with respect to cement microstructure: (a) 3D reconstruction of the crack surface area and porosity in the microspecimen in the stage 'B' shown in 2D in Figure 3b; (b) 3D reconstruction of the major tensile crack in the microspecimen in the stage 'B' showing the areas (dark purple colour) in which the crack intersects the unhydrated cement particles.

6 CONCLUSION

In this paper we present the results of some preliminary microtensile experiments. Synchrotron-based microtomography in combination with quantitative 3D image analysis revealed details of the fracture process in cement samples of extremely small size. Due to the constraints in the microtomography set-up, the experiments were not stable,

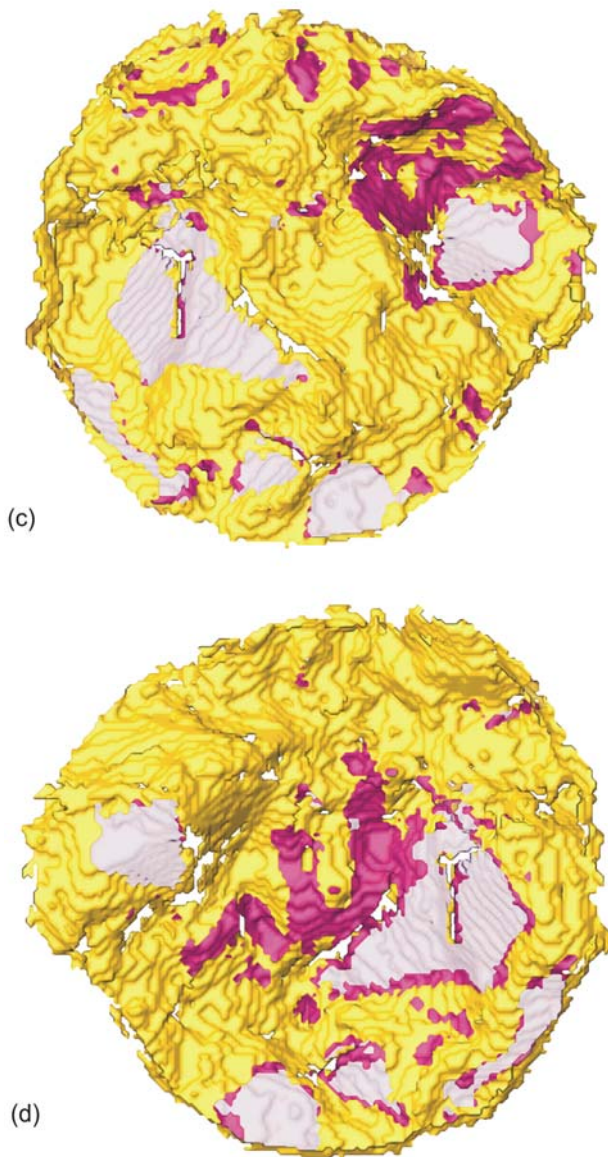


Figure 4c-d. Top-down and bottom-up views of the 3D reconstruction of the crack shown in Figure 4b. The parts of crack surfaces contacting the unhydrated cement particles made as partially translucent. *Yellow* – top crack surface contacting hydration products, *Light purple* – top crack surface in contact with unhydrated cement particle, bottom crack surface in contact with hydration product (i.e. crack through interface of the hydration products and unhydrated particles), *Light pink* – both crack surfaces in contact with unhydrated cement particle, *White islands* – crack bridges connecting the two specimen halves.

and no load-displacement diagrams were measured. However, the experiments revealed what happened before and after critical crack growth. Since similar bridging and branching phenomena were observed comparable to those found in concrete at the meso- and macro-scale, it can be deduced that hardened cement paste is a quasi-brittle material (i.e. shows softening) at the scale of observation ($[\mu\text{m}]$ -scale). Moreover, it can be concluded that the unhydrated

kernels of partially hydrated cement grains do not act like rigid stiff sand and gravel particles in concrete at the meso- and macro-scale. Due to the clearly visible internal structure of some of the unhydrated cement kernels, cracks were found to propagate through all phases of the cement. Identification of the properties of all relevant phases is essential for developing micro-structural mechanics models like we did in the past for concrete (Lilliu & van Mier (2003)).

ACKNOWLEDGEMENTS

The authors would like to acknowledge contributions of Messrs Cornelius Senn, Jürg Inhelder, Martin Suter and Heinz Richner – technicians at the Institute for Building Materials, ETH Zurich. Mr Christoph Hauri, Institute for Quantum Electronics, ETH Zurich is thanked for help with femtosecond laser part of the experiment. Contributions of Dr Paul Beaud and Dr Amela Grošo (both Paul Scherrer Institute, Villigen) are also gratefully acknowledged.

REFERENCES

- Constantinides, G. & Ulm, F.J. 2004. The effect of two types of C-S-H on the elasticity of cement-based materials: Results from nanoindentation and micromechanical modeling. *Cem. & Concr. Res.* 34, 67-80
- Diamond, S. 2004a. Special issue on scanning electron microscopy of cements and concretes. *Cem.Conc.Comp.* 26: 917-918.
- Diamond, S. 2004b. The microstructure of cement paste and concrete - a visual primer. *Cem.Conc.Comp.* 26: 919-933.
- Gonzalez, R.C. & Woods, R.E. 2002. *Digital Image Processing*. Upper Saddle River, NJ, USA, Prentice Hall.
- Herrmann, H.J., Hansen, A. & Roux, S. 1989. Fracture of disordered, elastic lattices in 2 dimensions. *Phys.Rev.B* 39: 637-648.
- Lilliu, G. & van Mier, J.G.M. 2003. 3D-lattice type fracture model for concrete. *Eng.Fract.Mech.* 70: 927-941.
- Schuh, C. A., Mason J. K. & Lund A. C. 2005. Quantitative insight into dislocation nucleation from high-temperature nanoindentation experiments. *Nature Mater.* 4: 617-621.
- Scrivener, K.L. 2004. Backscattered electron imaging of cementitious microstructures: understanding and quantification. *Cem.Conc.Comp.* 26: 935-945.
- Scrivener, K.L. 1984. *The Development of Microstructure during the Hydration of Portland Cement*. PhD-thesis, Imperial College, London.
- Snigirev, A., Snigireva, I., Kohn, V., Kuznetsov, S. & Schelokov, I. 1999. On the possibilities of X-ray phase contrast micro-imaging by coherent high-energy synchrotron radiation. *Rev. Sci. Inst.* 66: 5486-5492
- Stampanoni, M., Borchert, G., Wyss, P., Abela, R., Patterson, B., Hunt, S., Vermeulen, D. & Rueggsegger 2002. High resolution X-ray detector for synchrotron-based microtomography. *Nucl. Inst. & Meth. A* 491: 291-301.
- van Mier, J.G.M. 1991. Mode I fracture of concrete: Discontinuous crack growth and crack interface grain bridging. *Cem. Concr.Res.* 21: 1-15.

- van Vliet, M.R.A. & van Mier, J.G.M. 2000. Experimental investigation of size effect in concrete and sandstone under uniaxial tension. *Eng.Fract.Mech.* 65: 165-188.
- Velez, K., Maximilien, S., Damidot, D., Fantozzi, G. & Sorrentino, F. 2001. Determination by nanoindentation of elastic modulus and hardness of pure constituents of Portland cement clinker. *Cem.Concr.Res.* 31: 555-561.
- Xu, A.M. & Sarkar, S.L. 1991. Microstructural study of gypsum activated fly-ash hydration in cement paste. *Cem.Conc. Res.* 21: 1137-1147.

APPENDIX: METHODS

Sample preparation. As a cylinder is the most convenient specimen shape from the tomography point of view, all the samples used were microcylinders produced from Portland cement CEM I 42.5 N with water/cement ratio equal to 0.33. Special coupons, made of polytetrafluorethylen (PTFE) sheets of 250 μm in thickness with apertures of 130 μm in diameter, were developed for their production. The samples were cast in such a manner that the whole coupon was submerged into the fresh cement paste, while being held in tweezers. Having been removed from the fresh paste, the coupons were then placed in a small plastic bag that was stored in a climate box at 25°C and 75% R.H. After curing the specimens for 6 days, the thin layers of material on the top and the bottom of the coupon was carefully removed, leaving the microcylinders of 130 μm in diameter and approximately 250 μm in height embedded in the PTFE coupon. The samples were then carefully demoulded under an optical microscope by cutting the PTFE sheet away using a sharp razor blade. The samples were then axisymmetrically glued onto short tungsten needles of 130 μm in diameter using a glue hardening under UV light. This needle later became one of the parts of the microtensile device. In this state a notch has been machined in the centre of the specimen using femtosecond laser pulses of 100 fs pulse length, 4 μJ pulse energy, 100 Hz repetition rate.

Synchrotron radiation x-ray computed microtomography (SR μ CT). Tomographic investigations have been performed at an X-ray wavelength of 1 Å, selected with a Si111 monochromator from the wiggler source of the Materials Science beamline of the Swiss Light Source. The magnification of the detector was set to 40x and the CCD chip was binned resulting in a theoretical pixel size of 0.7 microns and a very good signal to noise ratio. Since the specimen (130 microns) was filling the field-of-view (720 microns) by less than one third, the requirements of the sampling theorem could be relaxed and only 401 angular projections have been acquired. With an exposure time of 2 seconds per image, the total scan time was approximately 20 minutes. Sample-to-detector distance has been minimized in order to reduce the

formation of Fresnel fringes (Snigirev et al. (1999)), which can affect the spatial resolution.

Image Analyses. 3D image analysis consisted of three basic steps: threshold-based segmentation, identification of connected objects, and measurement of object properties. The threshold level used for segmentation was determined from the voxel intensity histogram. The histograms for these specimens were trimodal, consisting of voxel distributions representing void (darkest), hydrated cement phases (darker grey), and unhydrated cement particles (lighter grey). The threshold used to separate void space from solid is then taken as the local minimum between the two adjacent peaks on the histogram, minimizing the error associated with mislabelling a voxel, see Gonzalez & Woods (2002). The remaining steps are to identify and measure all the resulting void objects in the 3D space. This was done using an efficient connected components algorithm, which labels and measures the surface area and volume of each void object. Surface area is calculated by counting the number of free (not connected) voxel faces and multiplying by the unit voxel area. 3D displacement vectors were estimated using a block-matching method for intensity-based registration. Displacement vectors are calculated by finding the maximum cross correlation between a segment in the reference image (unloaded stage of the specimen) and a same-sized region in a larger search window in subsequent images (respective loaded stages of the specimen).